Electronic Supplementary Material (ESI) for Catalysis Science & Technology.
This journal is © The Royal Society of Chemistry 2022

Electronic Supplementary Information (ESI) *for*

# *Operando spectroscopy of a working room temperature nanocomposite methanol sensor*

Qaisar Maqbool[1], Nevzat Yigit[2], Michael Stöger-Pollach[3], Maria Letizia Ruello[1], Francesca Tittarelli[1], and Günther Rupprechter[2]*

*Correspondence to: guenther.rupprechter@tuwien.ac.at

**ESI includes:**

Supplementary Text S1 to S4
Figs. S1 to S14
Tables S1 to S4

## Supplementary Text

### S1: Powder Ultraviolet-visible (UV-vis) spectroscopy of rGO

Ultraviolet-visible spectroscopy of rGO in powder phase was performed using a UV/Vis spectrometer (Perkin Elmer Lambda 750). Due to GO reduction into rGO (Fig. S2), the electronic conjugation was restored which was observed as a persistent UV absorption above 270 nm. This behavior resembles materials such as few-layered graphene nanosheets obtained via high intensity sonication of graphite [1], and highly reduced rGO [2–4]. The UV results are also consistent with the HRTEM and XRD observations, validating few-layered and highly reduced rGO.

### S2: Energy Loss Near Edge Spectroscopy (ELNES) of $TiO_2$-NPs and HR-TEM of $TiO_2$@rGO-NC

Since both, rutile and anatase, have the same stoichiometry, chemical quantification via conventional scattering cross sections for the respective ionization edges cannot distinguish the two phases. On the other hand, their electronic structure differs especially for the Ti $L_{3,2}$-edge, which was recorded in detail. The energy-loss near edge structure (ELNES) reflects the density of states (DOS) above the Fermi level. The DOS itself depends on the crystallography and chemical environment of the detected chemical elements. In the case of $TiO_2$, the ELNES of the Ti $L_{3,2}$-edge can be used as a fingerprint for differentiating rutile and anatase. The recorded ELNES, as shown in Fig. S3A, is clearly characteristic of anatase-$TiO_2$.

**S3: Thermal analysis**

To examine a potential use of the prepared sensor materials at higher temperatures, their thermal properties were analyzed by TG, DTG and SDTA (Fig. 1E and Fig. S4). The temperature of maximum decomposition (Tn) within one weight loss step, the relative weight loss (Δm) and the decomposition temperature (Td), i.e., the temperature of 5% weight loss, are summarized in Table S3 for each material. To evaluate the effect of oxygen in the air, corresponding studies were first performed in $N_2$.

The thermal behavior of $TiO_2$-NPs in $N_2$ (Fig. S4) can be divided into three stages. The first endothermic stage from room temperature to 200 °C with a mass loss of 2.6% can be attributed to the evaporation of small molecules such as physically adsorbed water (dehydration) and removal of organic solvent residues. The further weight loss from 200°C to 600°, with a global exothermic behavior, may include $TiO_2$ phase transformation from anatase to rutile [5,6], thermal decomposition of the peroxo titanium complex and the oxidative decomposition of carbon based compounds with maximum degradation at T = 498°C. Beyond 600° C, the endothermic peak in the DTA curve (T3 ~750°C) without weight loss reflects the phase transformation of $TiO_2$ from anatase to rutile [6,7]. Overall, the sample had a total of 8.8% weight loss with a Td value of 425°C.

In air, the TG curves of $TiO_2$-NPs showed a similar behavior, but with less evident endothermic peaks since the presence of oxygen favors exothermic processes. In this case, the first weight loss attributed to the loss of small molecular compounds was 2.5%. Then, the thermal decomposition of the titanium complex and organic residues gave rise to 2.1% and 1.4% weight loss at Tn´s of 287°C and 452°C, respectively, followed by the phase transition from anatase to rutile without significant weight loss. In total, the $TiO_2$-NPs lost 7.35% weight in air and Td was 404°C.

For rGO, in the presence of air (Fig. S4), the mass loss occurred in a single main step. First, up to 400°C, a slight weight decrease occurred due to the loss of VOCs and water with possibly back-to-back endo and exothermal processes. Then, at T>400°C, due to the presence of oxygen, a sharp oxidative decomposition occurred with an exothermic peak at T = 531°C and weight loss of 88%. At T>600°C, no further weight loss was recorded. The total mass loss of rGO in air was 97% and Td was 295°C.

In $N_2$, the weight loss of rGO due to pyrolysis was more gradual then under air. At first, VOCs and water were lost up to 150°C (T1 = 49°C). Then, thermal decomposition of organic compounds occurred which overlapped with exothermic peaks with a maximum weight loss at T = 270°C. Td was 290°C. At 1000°C, the residual weight (75%) in $N_2$ was higher than for RGO in air due to additional residuals of unburned char. Moreover, TG in $N_2$, differently from TG in air, showed a continuous weight decrease even at T >1000°C. Decomposition of rGO in $N_2$ primarily depended on the available functional oxygen groups. When compared to literature, the rGO of the current study was a highly reduced form of GO with least available $O_2$ species and stronger van der Waals forces between the layers [8] thus providing higher thermal stability and some resistance to pyrolysis at high temperature.

For thermal analysis results of $TiO_2$@rGO-NC in air see the main text (Fig. 1E). In brief, the $TiO_2$@rGO-NC was thermally stable up to at least 300°C, making it compatible with high temperature sensing. In $N_2$, only the Δm at T3 was significantly lower due to the absence of oxygen.

**S4: BET Surface area**

For rGO, the hysteresis loop appeared (Fig. S5) at relative high pressure ($p/p^0$), fitting best a type-III isotherm model, which reflects the hydrophobic nature of rGO as adsorbent. Such adsorption behavior is typical for adsorbate–adsorbate interaction being larger than adsorbate–sorbent interaction, e.g., water adsorption on hydrophobic surfaces (zeolites or activated carbon) [9]. On the other hand, for $TiO_2$-NPs and 50% $TiO_2$@rGO-NC the characteristic H3-hysteresis loop fits the type-IV isotherm model [10]. The BET surface area of $TiO_2$-NPs, rGO and 50% $TiO_2$@rGO-NC were 101.5 $m^2/g$, 36.4 $m^2/g$ and 70.8 $m^2/g$, respectively. Moreover, BJH cumulative pore volume and pore width of $TiO_2$-NPs, rGO and 50% $TiO_2$@rGO-NC were 0.11 $cm^3/g$ - 5.9 nm,0.13 $cm^3/g$ - 37.4 nm and 0.08 $cm^3/g$ - 6.8 nm, respectively. A high surface area, small and homogenous particle size of the green synthesized $TiO_2$-NPs are beneficial for their methanol gas sensing performance. Usually, metal oxide NPs with high surface area exhibit better sensitivity towards methanol sensing, which comes, however, with the limitation of higher working temperature [11]. Contrary, our study reports that $TiO_2$-NPs with high surface area (101.5 $m^2/g$) can indeed be efficiently utilized for better understanding room temperature methanol sensing.

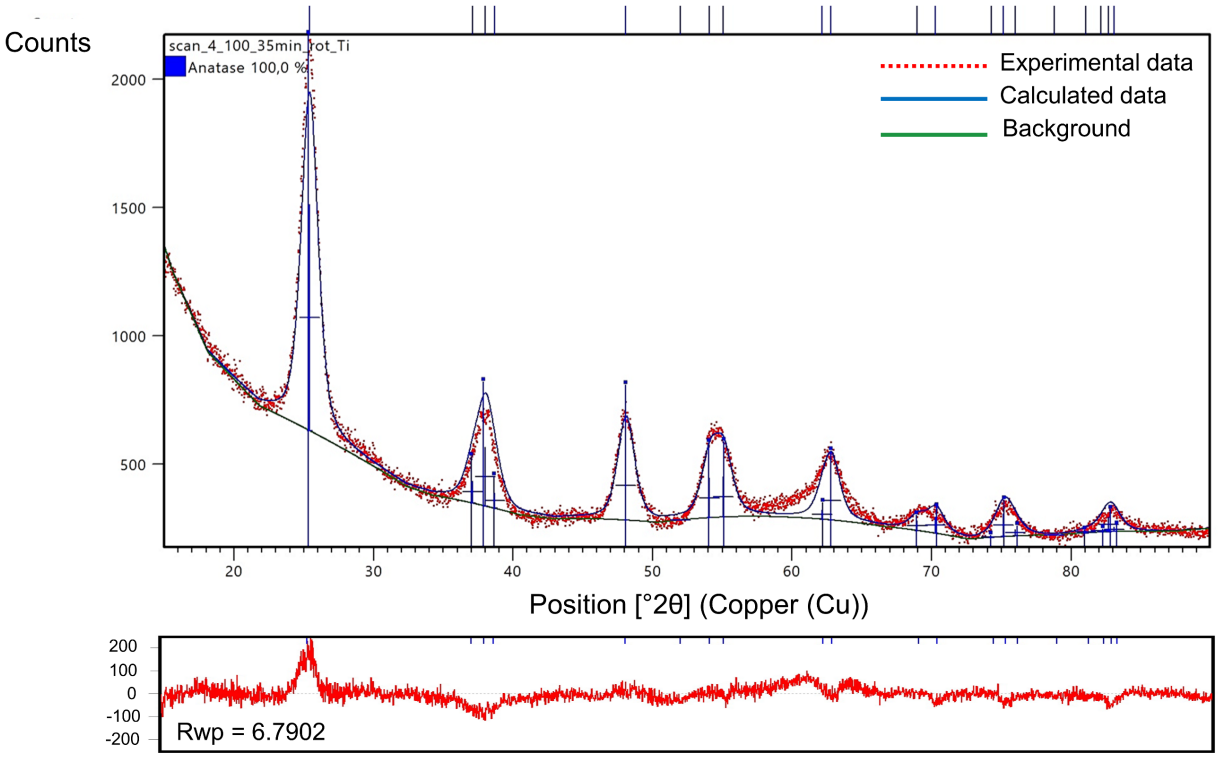


**Fig S1**. Rietveld refinement of $TiO_2$-NPs structure (XRD data) using HighScore Plus® (v2021) connected with ICDD® database (refined with ICDD 04-016-2837).

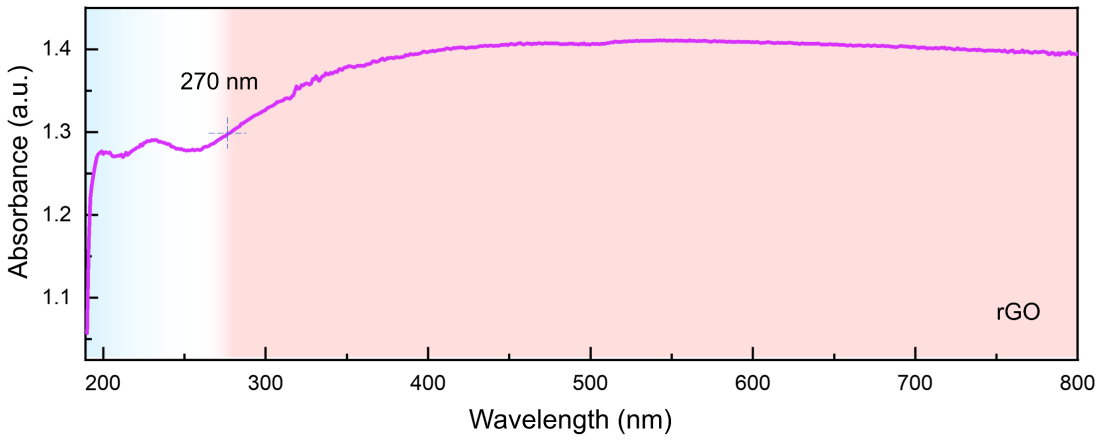


**Fig. S2.** UV-vis spectra (complete scan) of as synthesized rGO in powder phase showing continuous absorption above 270 nm due to reduction of GO to rGO.

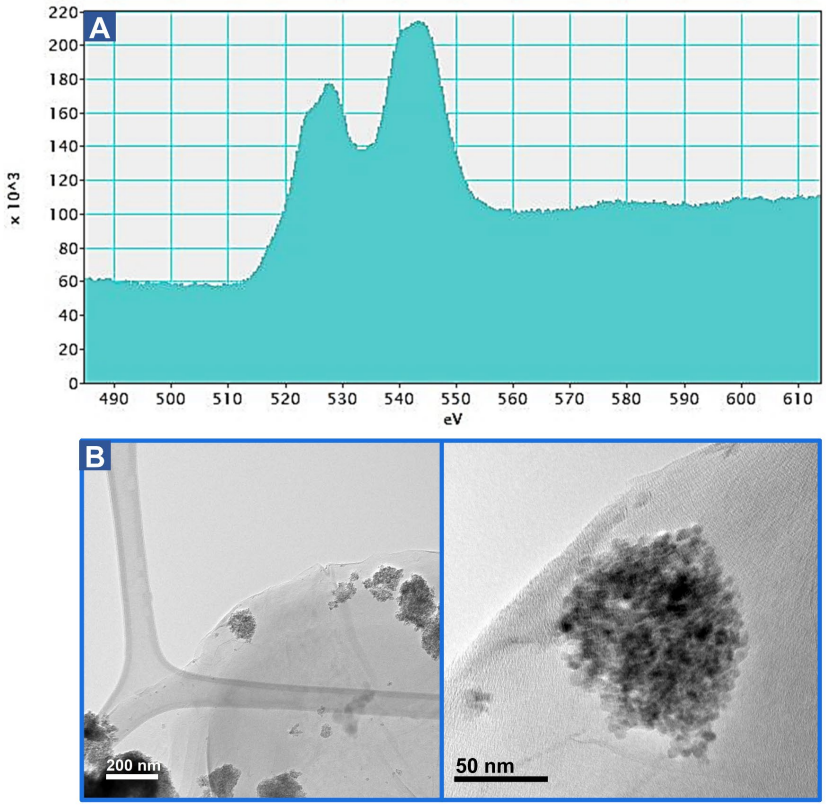


**Fig. S3. (A)** Energy Loss Near Edge Spectroscopy (ELNES) of synthesized Anatase-$TiO_2$-NPs. **(B)** HR-TEM of $TiO_2$@rGO-NC.

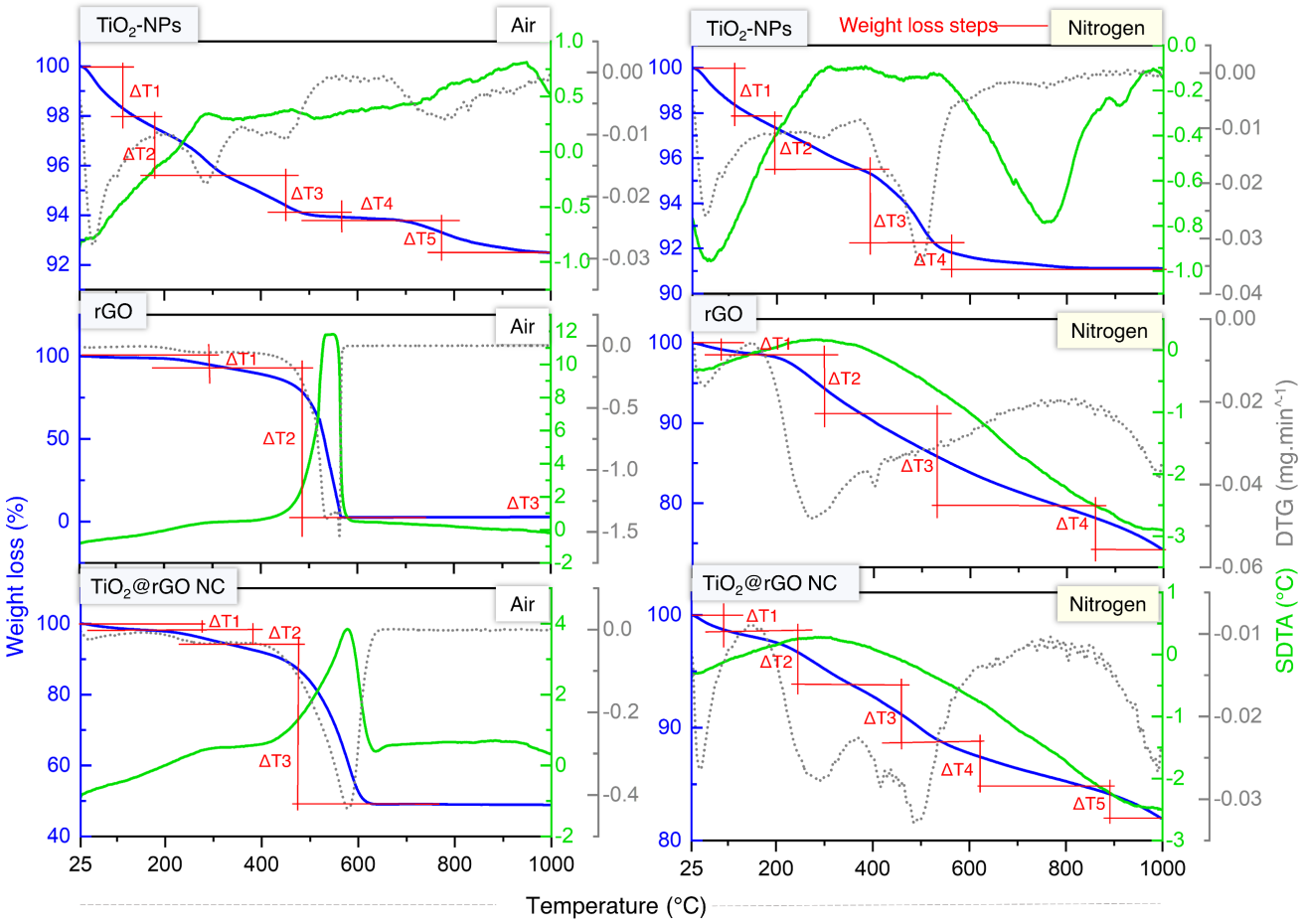


**Fig. S4.** TG (blue), DTG (grey) and SDTA (green) analysis of $TiO_2$-NPs, rGO and 50% $TiO_2$@rGO NC in air and nitrogen.

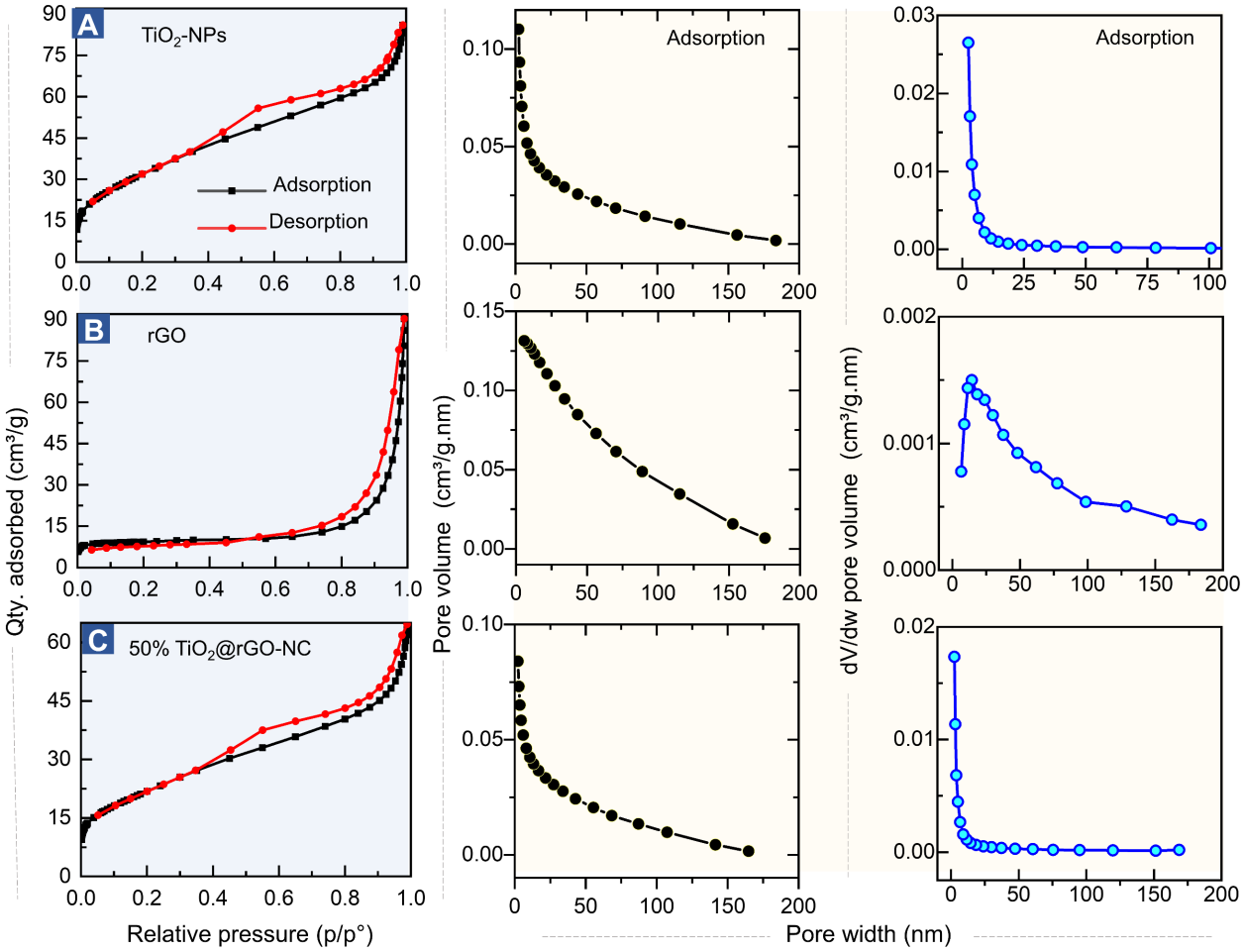


**Fig. S5.** BET $N_2$ adsorption-desorption isotherms (left) and corresponding pore size distributions (middle and right) of **(A)** green synthesized $TiO_2$-NPs, **(B)** rGO and **(C)** $TiO_2$@rGO-NC.

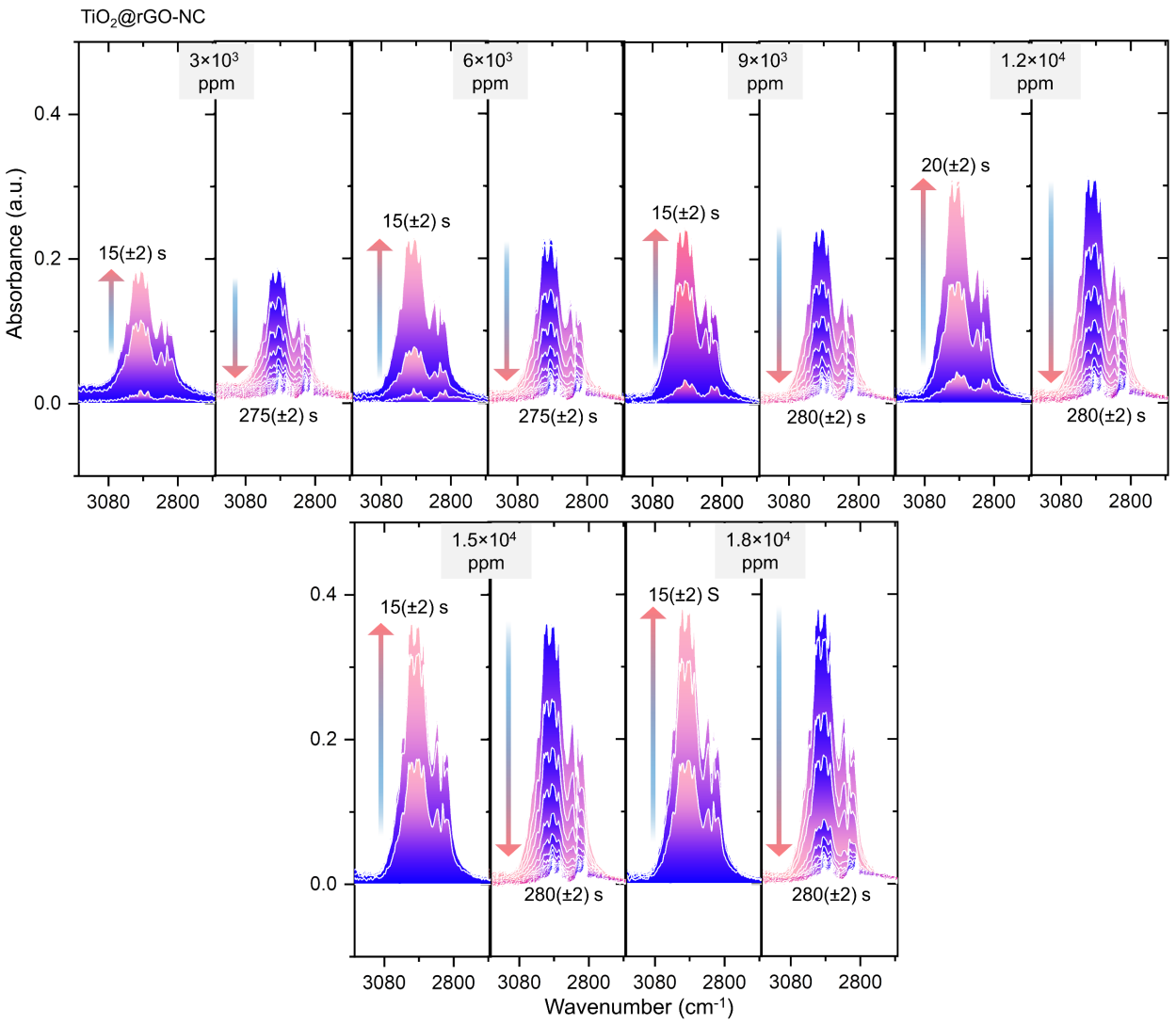


**Fig. S6.** Time-resolved DRIFTS of 50% $TiO_2$@rGO-NC, showing adsorption-desorption of methanol gas at different concentrations. The IR-derived response and recovery times are indicated.

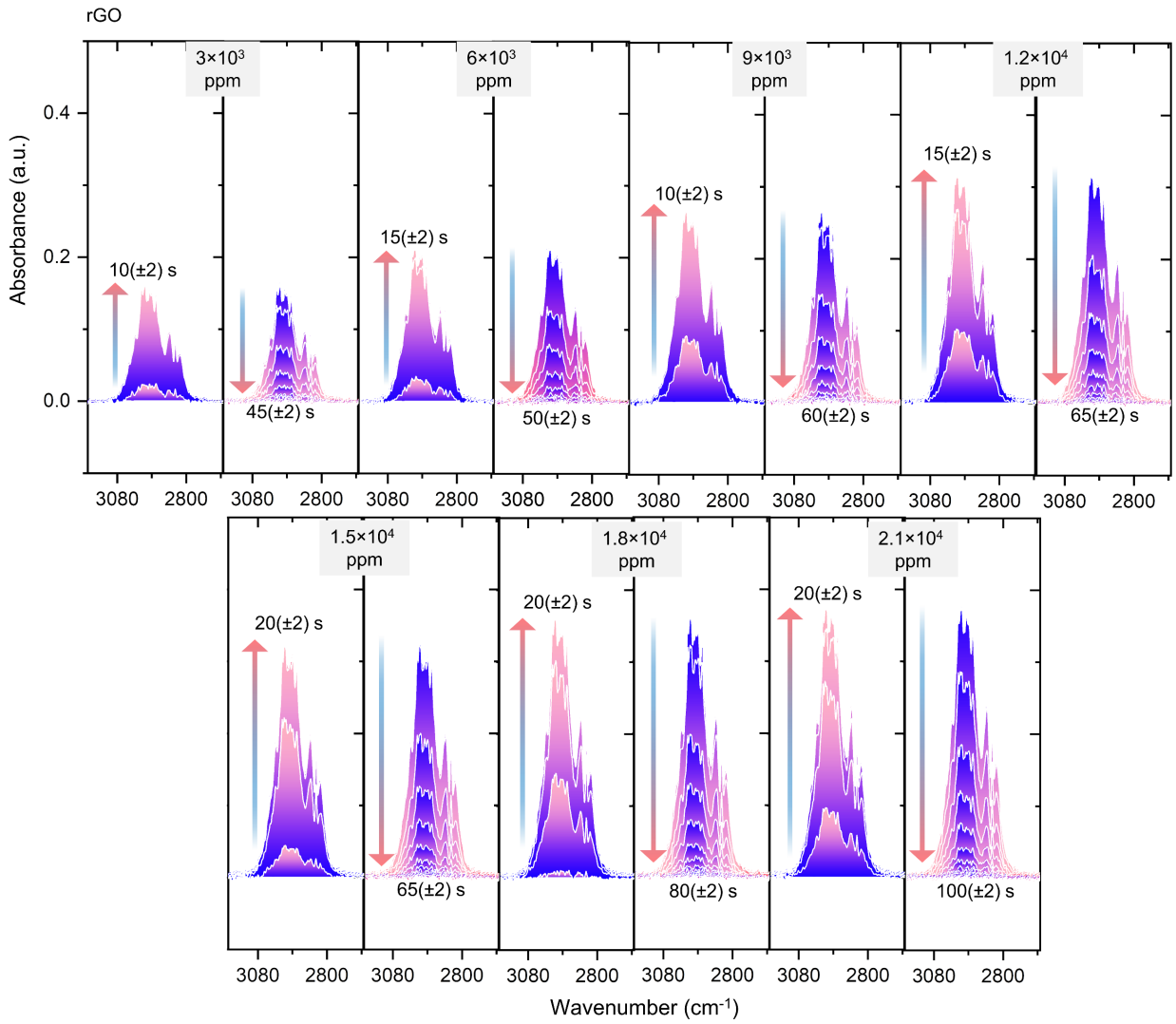


**Fig. S7.** Time-resolved DRIFTS of rGO, showing adsorption-desorption of methanol gas at different concentrations. The IR-derived response and recovery times are indicated.

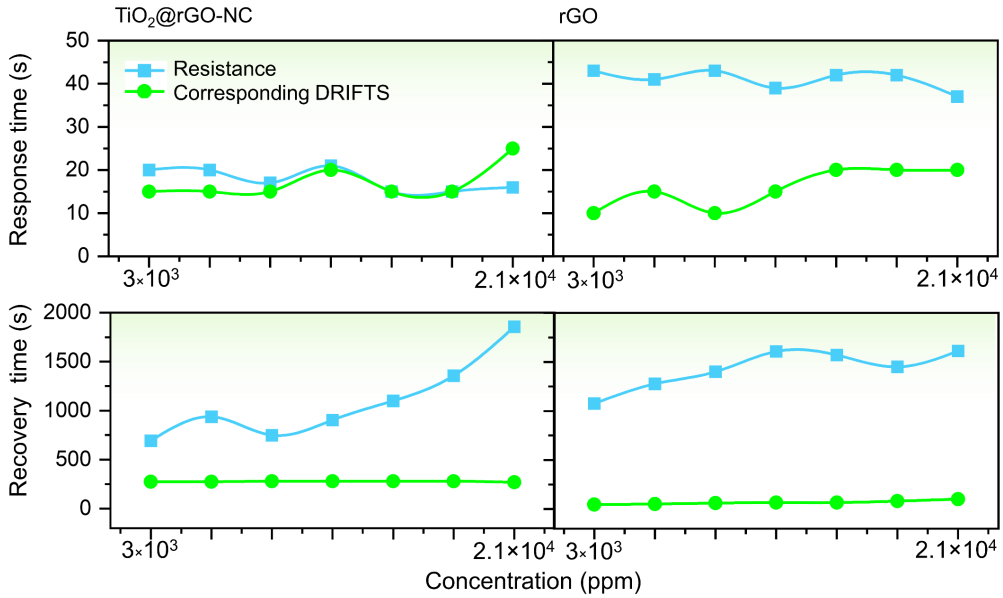


**Fig. S8.** Comparative analysis of sensor materials. Resistance vs. IR intensity changes, in terms of response and recovery times at different methanol concentrations ($3\times10^3$ - $2.1\times10^4$ ppm).

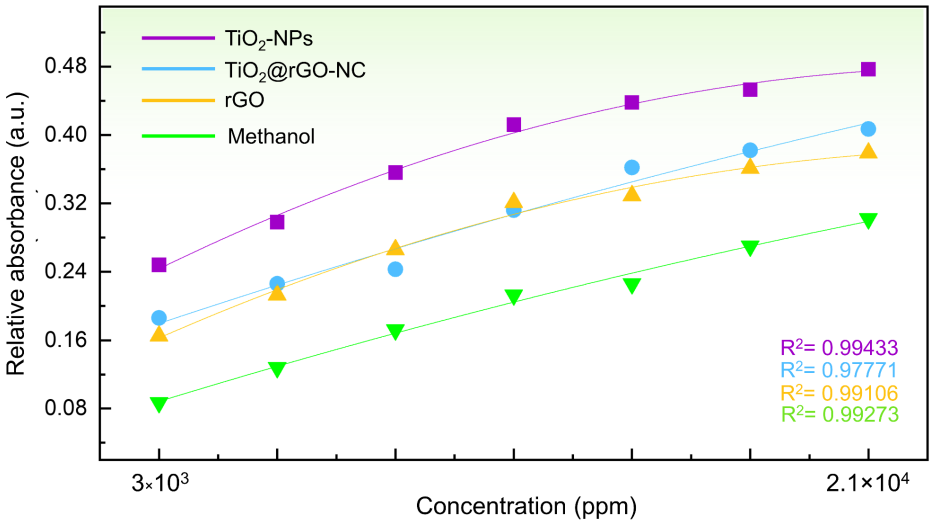


**Fig. S9.** Relative IR absorbance intensities for different methanol concentrations ($3\times10^3$ - $2.1\times10^4$ ppm), on various sensor materials.

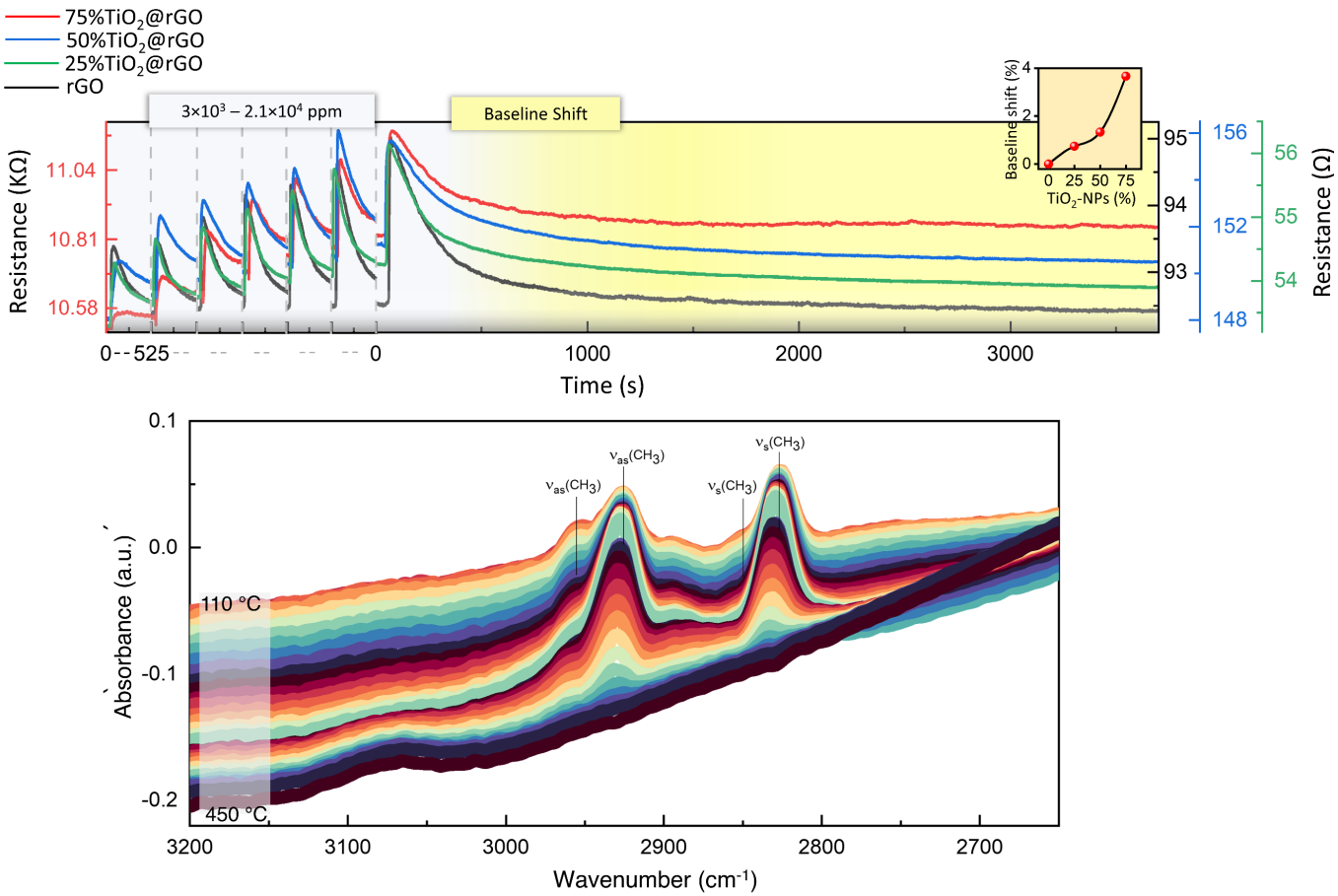


**Fig. S10.** Effect of $TiO_2$-NPs concentration (0-75%) in rGO on methanol sensing and initial baseline shift. The inset shows that the baseline shift increases for higher fraction of $TiO_2$-NPs. (Bottom) Temperature programmed desorption (TPD) of surface adsorbed methanol on $TiO_2$-NPs monitored by DRIFTS.

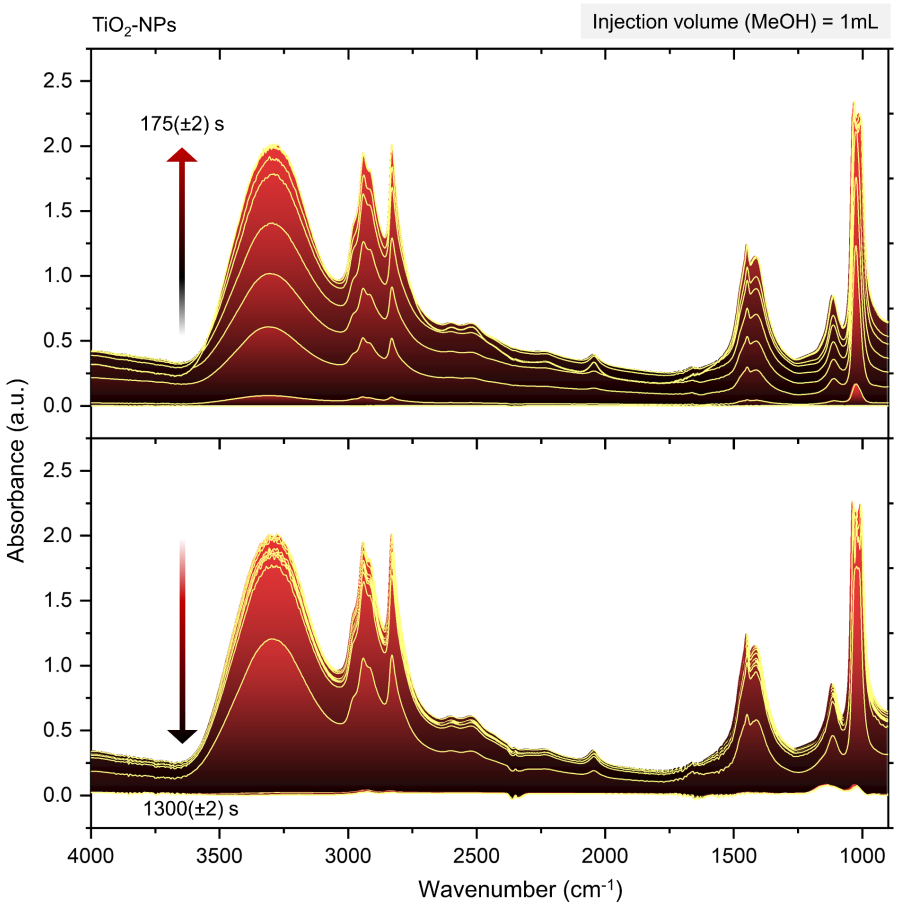


**Fig. S11.** Time-resolved ATR-IR of $TiO_2$-NPs, showing adsorption-desorption of methanol. Spectra acquired in 5 s intervals.

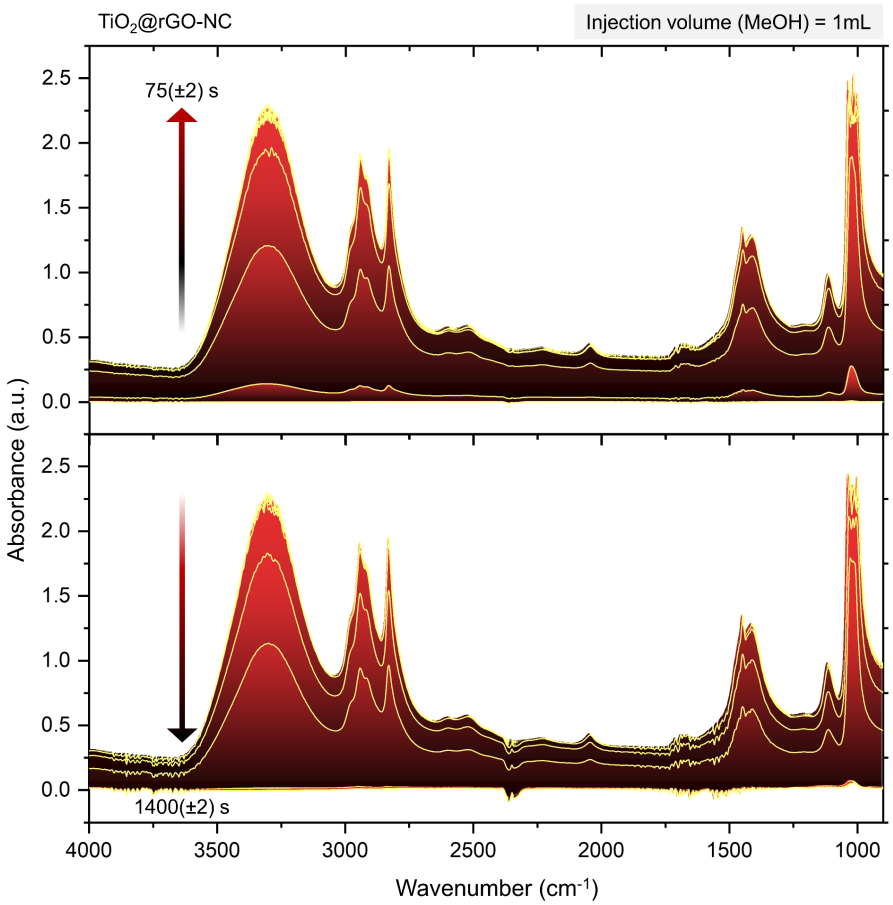


**Fig. S12.** Time-resolved ATR-IR of $TiO_2$@rGO-NC, showing adsorption-desorption of methanol. Spectra acquired in 5 s intervals.

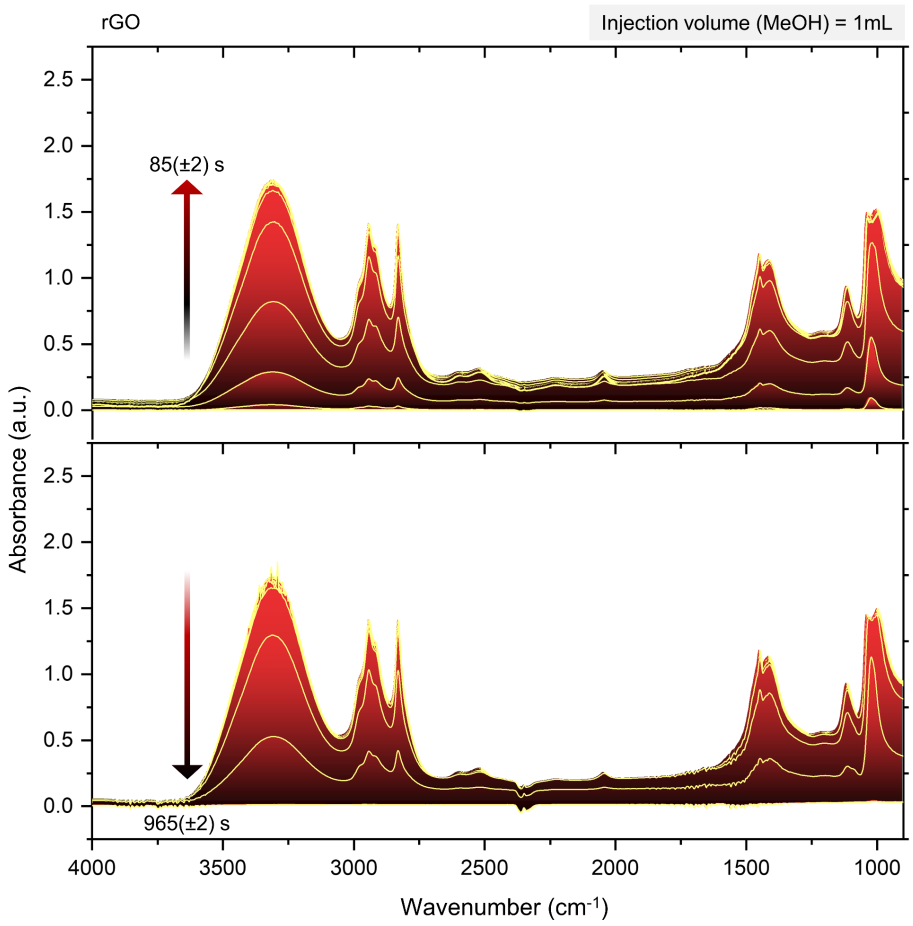


**Fig. S13.** Time-resolved ATR-IR of rGO, showing adsorption-desorption of methanol. Spectra acquired in 5 s intervals.

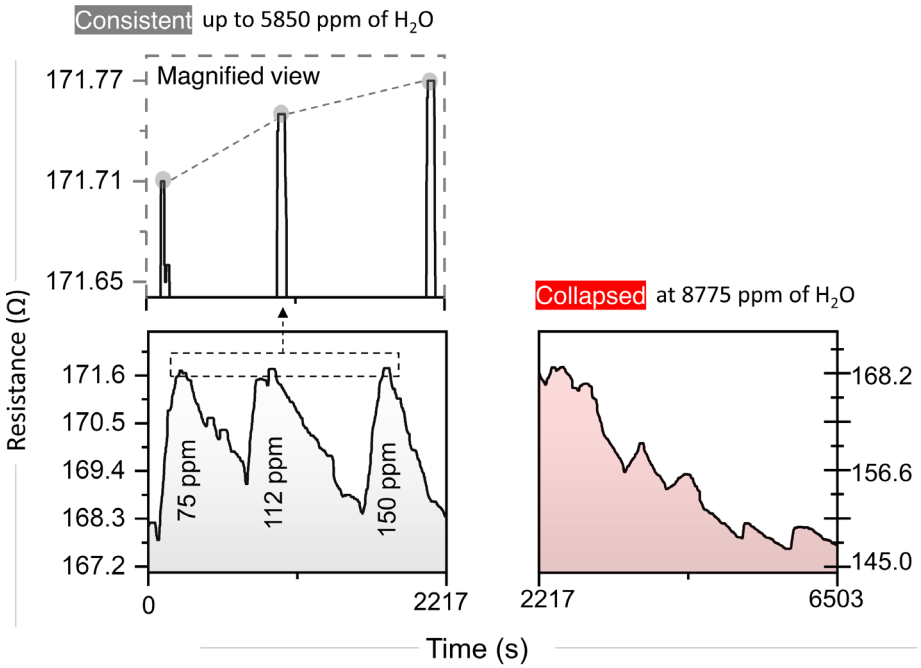


**Fig. S14.** Room temperature methanol detection by 50% $TiO_2$@rGO-NC at low methanol concentrations (75 to 150 ppm) and high humidity (2925 to 5850 ppm).

**Table S1.** Comparison of green synthesis methods, crystallographic and morphological properties of green synthesized $TiO_2$ nanoparticles.

| Biological material used | Precursor used | Particle size (nm) | Crystallite size (nm) | Morphology | Phase purity | Ref. |
|---|---|---|---|---|---|---|
| Organic waste (Olive leaves) | $TiOSO_4$. $xH_2SO_4$ | ≤ 6 | 4.1 | Spherical | Anatase | This work |
| *Syzygium cumini* (Fresh leaves) | $Ti[OCH(CH_3)_2]_4$ | 18 | 10 | Spherical/irregular | Anatase | [12] |
| *Withania somnifera* (Fresh roots) | $TiO_2$ | 40-100 | 45.3 | Spherical/porous | Anatase | [13] |
| *Citrus limetta* (Fresh leaves) | $Ti(OBu)_4$ | 80-100 | 45 | Spherical | Anatase | [14] |
| *Phyllanthus niruri* (Fresh leaves) | $Ti[OCH(CH_3)_2]_4$ | ≥ 100 | 20.9 | Irregular | Anatase | [15] |
| *Calotropis gigantea* (Fresh leaves) | $TiCl_4$ | 13-110 | 11.9 | Flower-like | Rutile | [16] |
| *Mangifera indica* L. (Fresh fruit peel) | $TiCl_3$ | 17-28 | 5.3-13.8 | Spherical/granular | Anatase-Rutile | [17] |
| *Pouteria campechiana* (Fresh leaves) | $TiO_2$ | 73-140 | 29 | Polydisperse | Anatase | [18] |
| *Ledebouria revoluta* (Fresh bulbs) | $TiO_2$ | 100-200 | 47 | Spherical | Rutile | [19] |
| *Cuminum cyminum* (Seeds) | $Ti[OCH(CH_3)_2]_4$ | 12.6 | 15.2 | Spherical/irregular | Anatase | [20] |
| *Monsonia burkeana* (Fresh plant) | $TiF_4$ | 6-10 | 8.9 | Spherical | Anatase | [21] |
| *Catharanthus roseus* (Fresh leaves) | $TiO_2$ | 25-110 | 100 | Irregular | Anatase | [22] |
| *Trigonella foenum* (Fresh leaves) | $TiOSO_4$. $xH_2SO_4$ | 20-90 | 25-30 | Spherical | Anatase | [23] |
| *Piper betel* (Dried leaves) | $Ti(OBu)_4$ | 8 | 4.0 | Spherical | Rutile | [24] |
| *Psidium guajava* (Fresh leaves) | $TiO(OH)_2$ | 32.6 | NA[1] | Spherical | Rutile/Anatase | [25] |

| | | | | | | |
|---|---|---|---|---|---|---|
| *Annona squamosa* (Fruit peel) | $TiO(OH)_2$ | 23 | NA[1] | Spherical/polydisperse | Rutile | [26] |
| *Jatropha curcas* L. (Crude latex) | $TiO(OH)_2$ | 25-100 | NA[1] | Spherical/irregular | Anatase | [27] |
| *Euphorbia prostrata* (Fresh leaves) | $TiO(OH)_2$ | 83.2 | NA[1] | Polydisperse | Anatase | [28] |
| *Sargassum myriocystum* (Fresh seaweed) | $TiO_2$ | ~50–90 | NA[1] | Irregular | Anatase | [29] |
| *Eclipta prostrata* (Fresh leaves) | $TiO(OH)_2$ | 36-68 | NA[1] | Spherical/polydisperse | Rutile | [30] |
| *Azadirachta indica* (Fresh leaves) | $Ti[OCH(CH_3)_2]_4$ | 124 | NA[1] | Spherical | NA[1] | [31] |

[1] NA= Not available (information not found)

**Table S2.** Crystallographic parameters of green synthesized anatase-$TiO_2$-NPs.

| **Peak pos. [°2Theta]** | | ***hkl*** | **FWHM[1]** | | **Crystallite size[2] [nm]** | | **Average crystallite size [nm]** | | **d- Spacing [nm]** | |
|---|---|---|---|---|---|---|---|---|---|---|
| **Raw data** | **Baseline corr.** | | **Raw data** | **Baseline corr.** | **Raw data** | **Baseline corr.** | **Raw data** | **Baseline corr.** | **Raw data** | **Baseline corr.** |
| 25.40 | 25.42 | 101 | 1.49 | 1.60 | 5.45 | 5.08 | 3.97 | 4.14 | 0.350 | 0.349 |
| 37.91 | 37.95 | 004 | 2.29 | 1.98 | 3.65 | 4.22 | | | 0.237 | 0.236 |
| 48.11 | 48.11 | 200 | 1.55 | 1.63 | 5.60 | 5.33 | | | 0.188 | 0.188 |
| 54.66 | 54.61 | 105 | 2.86 | 2.83 | 3.11 | 3.15 | | | 0.167 | 0.167 |
| 62.62 | 62.72 | 204 | 2.82 | 2.16 | 3.29 | 4.28 | | | 0.148 | 0.148 |
| 69.30 | 69.66 | 116 | 6.21 | 4.34 | 1.55 | 2.22 | | | 0.135 | 0.134 |
| 75.36 | 75.36 | 215 | 2.25 | 2.31 | 4.45 | 4.33 | | | 0.126 | 0.126 |
| 83.03 | 83.08 | 224 | 2.29 | 2.34 | 4.63 | 4.53 | | | 0.116 | 0.116 |

[1]FWHM were measured using Lorentz peak fitting for both raw data and after baseline correction using OriginPro® (V2021).
[2]Crystallite size were calculated using Scherrer equation

**Table S3.** Thermal properties for different sensor materials. The temperatures of maximum decomposition (Tn), the relative weight loss (Δm) and the temperature of 5% mass loss, defined as decomposition temperature (Td), are summarized for each material.

| **Sample** | **Properties** | **Air** | | | | | **Nitrogen** | | | | |
|---|---|---|---|---|---|---|---|---|---|---|---|
| | | **T1** | **T2** | **T3** | **Td** | **Total Δm %** | **T1** | **T2** | **T3** | **Td** | **Total Δm %** |
| $TiO_2$-NPs | Tn (°C) | 54 | 287 | 452 | 404 | 7.3 | 53 | 294 | 498 | 425 | 8.8 |
| | - Δm (%) | 2.5 | 2.1 | 1.4 | 5 | | 2.6 | 1.7 | 3.9 | 5.0 | |
| rGO | Tn (°C) | 531 | | | 295 | 97.0 | 49 | 270 | | 290 | 24.9 |
| | - Δm (%) | 88.0 | | | 5 | | 1.1 | 19.0 | | 5 | |
| 50% $TiO_2$@rGO NC | Tn (°C) | 44 | 290 | 576 | 314 | 51.0 | 43 | 292 | 488 | 319 | 17.8 |
| | - Δm (%) | 1.6 | 6.3 | 42.9 | 5 | | 1.6 | 4.8 | 7.6 | 5.0 | |

**Table S4.** Comparison of the room temperature methanol sensing performance and mechanism of the prepared sensors with previously reported materials.

| Sensing Material Description | Synthesis Method | Description of Sensing Mechanism | Response Time (s) | Detection Range (ppm) | Reversibility Test | Ref. |
|---|---|---|---|---|---|---|
| $TiO_2$@reduced graphene oxide nanocomposite | Green synthesis | *Operando* and *in situ* spectroscopy | 15 (100%) | 75 – $9\times10^5$ | Tested | This study |
| $TiO_2$ nanotubes | Anodic oxidation process | Wolkenstein adsorption-desorption theory | ≈50 (100%) | 100 - 300 | N/A | [32] |
| Graphene-doped polyaniline | Chemical oxidation | Theoretical fitting using Langmuir kinematic | 60 (100%) | 50 - 100 | Tested | [33] |
| 2D $Al_{\mu\text{-IDE}}/HfS_2$ | Chemical | Langmuir adsorption-desorption isotherm | ~12 (67%) | 100-500 | N/A | [34] |
| ZnO hexagonal nanotubes | Electrodeposition / Electrochemical etching | Langmuir-Hinshelwood isotherm | 144 (90%) | 10-700 | Tested | [35] |
| Multi-walled carbon nanotube/ polyaniline nanotube | Chemical | Density functional theory | 60 (100%) | 50 - 500 | Tested | [36] |
| Anatase $TiO_2$ quantum dots | Chemical | Comparing Inert gas ($N_2$) with $O_2$ environment | ≈200 (100%) | 1000 | Tested | [37] |
| $Ti_3C_2T_x$ (MXene) | Chemical | Hypothetical | ≈300 (100%) | 100 | Tested | [38] |
| Inkjet-printed polypyrrole | Physio-Chemical (polypyrrole over polyester) | Hypothetical | 40 (90%) | 5000 | Tested | [39] |
| Platinized mesoporous tungsten nitride | Solid state reaction | Hypothetical | 60 (90%) | 25-200 | Tested | [40] |
| Polyaniline-CdO nanocomposite | Chemical/ Co-precipitation / dip-coating | Hypothetical | 19 (90%) | 100 | N/A | [41] |
| $MnO_2$ and $V_2O_5$ doped Polyaniline | Chemical | Hypothetical | 110 (100%) | 40 - 60 | N/A | [42] |
| Carbon derivatives in poly(etherimide)–liquid crystal polymer composite | Chemical | Hypothetical | N/A | 300-1200 | Tested | [43] |
| $H_2SO_4$ doped poly (m-aminophenol) | Chemical | N/A | ≈140 (100%) | 173 - 330 | Tested | [44] |

| | | | | | | |
|---|---|---|---|---|---|---|
| PEDOT:PSS and $Ti_3C_2T_x$ (4:1) | Chemical | N/A | ≈300 (100%) | 300 | N/A | [45] |
| $In_2O_3$ over Au, Ag, Pt and Cu | Vapor deposition | N/A | N/A | 200 - 900 | N/A | [46] |

ppm = Part per million, N/A = Not available

**Supplementary References**


1 M. Noroozi, A. Zakaria, S. Radiman and Z. A. Wahab, *PLoS One*, 2016, **11**, e0152699.
2 B. A. Aragaw, *J. Nanostructure Chem. 2019 101*, 2019, **10**, 9–18.
3 S. Yang, W. Yue, D. Huang, C. Chen, H. Lin and X. Yang, *RSC Adv.*, 2012, **2**, 8827–8832.
4 C. P. P. Wong, C. W. Lai, K. M. Lee and S. B. Abd Hamid, *Mater. 2015, Vol. 8, Pages 7118-7128*, 2015, **8**, 7118–7128.
5 E. R. Spada, E. A. Pereira, M. A. Montanhera, L. H. Morais, R. G. Freitas, R. G. F. Costa, G. B. Soares, C. Ribeiro and F. R. de Paula, *J. Mater. Sci. Mater. Electron.*, 2017, **28**, 16932–16938.
6 X. Zhu, S. Han, W. Feng, Q. Kong, Z. Dong, C. Wang, J. Lei and Q. Yi, *RSC Adv.*, 2018, **8**, 14249–14257.
7 M. M. Mahlambi, A. K. Mishra, S. B. Mishra, R. W. Krause, B. B. Mamba and A. M. Raichur, *J. Therm. Anal. Calorim.*, 2012, **110**, 847–855.
8 T. Tene, G. T. Usca, M. Guevara, R. Molina, F. Veltri, M. Arias, L. S. Caputi and C. V. Gomez, *Nanomater. 2020, Vol. 10, Page 279*, 2020, **10**, 279.
9 M. A. Al-Ghouti and D. A. Da'ana, *J. Hazard. Mater.*, 2020, **393**, 122383.
10 S. Subudhi, G. Swain, S. P. Tripathy and K. Parida, *Inorg. Chem.*, 2020, **59**, 9824–9837.
11 Q. Rong, Y. Zhang, J. Hu, K. Li, H. Wang, M. Chen, T. Lv, Z. Zhu, J. Zhang and Q. Liu, *Sci. Reports 2018 81*, 2018, **8**, 1–12.
12 N. K. Sethy, Z. Arif, P. K. Mishra and P. Kumar, *Green Process. Synth.*, 2020, **9**, 171–181.
13 N. A. Al-Shabib, F. M. Husain, F. A. Qais, N. Ahmad, A. Khan, A. A. Alyousef, M. Arshad, S. Noor, J. M. Khan, P. Alam, T. H. Albalawi and S. A. Shahzad, *Front. Microbiol.*, 2020, **11**, 1680.
14 G. Nabi, A. Majid, A. Riaz, T. Alharbi, M. Arshad Kamran and M. Al-Habardi, *Inorg. Chem. Commun.*, 2021, **129**, 108618.
15 A. Panneerselvam, J. Velayutham and S. Ramasamy, *IET Nanobiotechnology*, 2021, **15**, 164–172.
16 P. Naresh Kumar Reddy, D. P. M. D. Shaik, V. Ganesh, D. Nagamalleswari, K. Thyagarajan and P. Vishnu Prasanth, *Appl. Surf. Sci.*, 2021, **561**, 150092.
17 I. N. Isnaeni, Indriyati, Dedi, D. Sumiarsa and I. Primadona, *Mater. Lett.*, 2021, **294**, 129792.
18 M. Narayanan, P. G. Devi, D. Natarajan, S. Kandasamy, K. Devarayan, M. Alsehli, A. Elfasakhany and A. Pugazhendhi, *Environ. Res.*, 2021, **200**, 111333.
19 R. Aswini, S. Murugesan and K. Kannan, *https://doi.org/10.1080/03067319.2020.1718668*, 2020, **101**, 2926–2936.
20 S. S. Mathew, N. E. Sunny and V. Shanmugam, *Inorg. Chem. Commun.*, 2021, **126**, 108485.
21 N. M. Ngoepe, M. M. Mathipa and N. C. Hintsho-Mbita, *Optik (Stuttg).*, 2020, **224**, 165728.
22 K. Velayutham, A. A. Rahuman, G. Rajakumar, T. Santhoshkumar, S. Marimuthu, C. Jayaseelan, A. Bagavan, A. V. Kirthi, C. Kamaraj, A. A. Zahir and G. Elango, *Parasitol. Res.*, 2012, **111**, 2329–2337.
23 S. Subhapriya and P. Gomathipriya, *Microb. Pathog.*, 2018, **116**, 215–220.

24 S. M. Hunagund, V. R. Desai, J. S. Kadadevarmath, D. A. Barretto, S. Vootla and A. H. Sidarai, *RSC Adv.*, 2016, **6**, 97438–97444.
25 T. Santhoshkumar, A. A. Rahuman, C. Jayaseelan, G. Rajakumar, S. Marimuthu, A. V. Kirthi, K. Velayutham, J. Thomas, J. Venkatesan and S. K. Kim, *Asian Pac. J. Trop. Med.*, 2014, **7**, 968–976.
26 S. M. Roopan, A. Bharathi, A. Prabhakarn, A. Abdul Rahuman, K. Velayutham, G. Rajakumar, R. D. Padmaja, M. Lekshmi and G. Madhumitha, *Spectrochim. Acta Part A Mol. Biomol. Spectrosc.*, 2012, **98**, 86–90.
27 M. Hudlikar, S. Joglekar, M. Dhaygude and K. Kodam, *Mater. Lett.*, 2012, **75**, 196–199.
28 A. A. Zahir, I. S. Chauhan, A. Bagavan, C. Kamaraj, G. Elango, J. Shankar, N. Arjaria, S. M. Roopan, A. A. Rahuman and N. Singh, *Antimicrob. Agents Chemother.*, 2015, **59**, 4782–4799.
29 P. Balaraman, B. Balasubramanian, W. C. Liu, D. Kaliannan, M. Durai, H. Kamyab, M. Alwetaishi, V. Maluventhen, V. Ashokkumar, S. Chelliapan and A. Maruthupandian, *Environ. Res.*, 2022, **204**, 112278.
30 G. Rajakumar, A. A. Rahuman, B. Priyamvada, V. G. Khanna, D. K. Kumar and P. J. Sujin, *Mater. Lett.*, 2012, **68**, 115–117.
31 R. Sankar, K. Rizwana, K. S. Shivashangari and V. Ravikumar, *Appl. Nanosci.*, 2015, **5**, 731–736.
32 P. Bindra and A. Hazra, *Sensors Actuators B Chem.*, 2019, **290**, 684–690.
33 R. Pal, S. L. Goyal, I. Rawal and S. Sharma, *Iran. Polym. J. (English Ed.*, 2020, **29**, 591–603.
34 S. Das, S. Sharma and S. K. Sharma, *IEEE Sens. J.*, 2019, **19**, 9090–9096.
35 D. Acharyya and P. Bhattacharyya, *Sensors Actuators B Chem.*, 2016, **228**, 373–386.
36 A. Bora, K. Mohan, D. Pegu, C. B. Gohain and S. K. Dolui, *Sensors Actuators B Chem.*, 2017, **253**, 977–986.
37 A. Šutka, R. Eglitis, A. Kuzma, K. Smits, A. Zukuls, J. D. Prades and C. Fàbrega, *ACS Appl. Nano Mater.*, 2021, **4**, 2522–2527.
38 E. Lee, A. Vahidmohammadi, B. C. Prorok, Y. S. Yoon, M. Beidaghi and D. J. Kim, *ACS Appl. Mater. Interfaces*, 2017, **9**, 37184–37190.
39 M. F. Mabrook, C. Pearson and M. C. Petty, *Sensors Actuators B Chem.*, 2006, **115**, 547–551.
40 D. Meng, S. Zhang, T. Thomas, C. Huang, J. Zhao, R. Zhao, Y. Shi, F. Qu and M. Yang, *Sensors Actuators B Chem.*, 2020, **307**, 127686.
41 R. Paulraj, P. Shankar, G. K. Mani, L. Nallathambi and J. B. B. Rayappan, *J. Electron. Mater. 2018 4710*, 2018, **47**, 6000–6006.
42 R. Pal, S. L. Goyal and S. Sharma, *AIP Conf. Proc.*, 2019, **2115**, 030217.
43 S. Bag, K. Rathi and K. Pal, *Nanotechnology*, 2017, **28**, 205501.
44 P. Kar, N. C. Pradhan and B. Adhikari, *Sensors Actuators B Chem.*, 2009, **140**, 525–531.
45 X. Wang, K. Sun, K. Li, X. Li and Y. Gogotsi, *Chinese Chem. Lett.*, 2020, **31**, 1018–1021.
46 N. G. Patel, P. D. Patel and V. S. Vaishnav, *Sensors Actuators B Chem.*, 2003, **96**, 180–189.